Generalized Finite Element Analysis of Three-Dimensional Heat Transfer Problems Exhibiting Sharp Thermal Gradients

P. O'Hara[†], C.A. Duarte[†] and T. Eason[‡]

[†]Department of Civil and Environmental Engr., University of Illinois at Urbana-Champaign,
Newmark Laboratory, 205 North Mathews Avenue, Urbana, Illinois 61801, USA
e-mails: {pohara,caduarte}@uiuc.edu

[‡]Air Force Research Laboratory
Air Vehicles Directorate, WPAFB, Ohio, USA,
e-mail: Thomas.Eason@wpafb.af.mil

Abstract

In this paper, heat transfer problems exhibiting sharp thermal gradients are analyzed using the classical and generalized finite element methods. The effect of solution roughness on the ability of the methods to obtain accurate approximations is investigated. Convergence studies show that low order (linear and quadratic) elements require strongly refined meshes for acceptable accuracy.

We propose a generalized FEM with global-local enrichments for the class of problems investigated in the paper. In this procedure, a global solution space defined on a coarse mesh is enriched through the partition of unity framework of the generalized FEM with solutions of local boundary value problems. The local problems are defined using the same procedure as in the global-local FEM, where boundary conditions are provided by a coarse scale global solution. Coarse, uniform, global meshes are acceptable even at regions with thermal spikes that are orders of magnitude smaller than the element size. Convergence on these discretizations was achieved even when no or limited convergence was observed in the local problems. Two approaches are proposed to improve the boundary conditions prescribed on local problems and their convergence. The use of the corresponding improved local solutions as enrichments for the global problem extends the range of target error level for the enriched global problem.

The two-way information transfer provided by the proposed generalized FEM is appealing to several classes of problems, especially those involving multiple spatial scales. The proposed methodology brings the benefits of generalized FEM to problems were limited or no information about the solution is known a-priori.

1 Introduction

Many applications in engineering practice involve the analysis of structural behavior with multiple spatial scales of interest. One such case is seen in structures subjected to intense loadings of a localized nature. The motivation for this particular investigation is the analysis of localized heat sources on the skin of hypersonic flight vehicles. The methodology proposed here, however, may be applied to any of a number of practical situations involving intense, and highly localized heat sources, such as in the case of laser heating and welding, to name only a few.

Vehicles in hypersonic flight are subjected to very severe thermo-mechanical loadings (only the thermal loadings are considered here). At very high speeds, there are significant changes in the properties of the

compressed air, such as the density and temperature [41]. Changes in the pressure distributions on a hypersonic flight vehicle can cause the formation of shock waves in specific locations. Possible interactions of these shock waves can cause very intense thermal loadings, which are very localized and exhibit sharp gradients. The characterization of the resulting thermal loadings and pressure distributions, as well as the effect of these loadings on the aeroelastic behavior of the vehicle itself has been the focus of many research investigations [7, 23, 24, 32, 44, 45, 47]. The most severe of these loadings is the so-called Edney Type IV shock wave interaction, which is a bow shock/cowl shock interaction which may occur on the leading edge of a wing. Attempts have also been made to take into account the chemistry of the high-speed flow field itself [25] and to develop a fully analytical solution for the Type IV interaction [22]. A nice summary of the research performed in the area of high-speed air-vehicles can be found in [41].

Several investigations have been performed into the numerical solutions of heat transfer problems with localized effects, similar to the type of problems of interest in this work. Tamma and Saw offer [27] a local, hierarchical *p*-enrichment strategy for thermal problems in which a-posteriori error estimates are used to drive the local *p*-enrichment in elements whose error level is deemed unacceptable. The effects of localized, intense laser irradiation on a functionally graded composite plate is investigated in [5], using a Meshless Local Petrov-Galerkin Method. The effects of heat generated due to dynamic fracture in an elastic-plastic medium is investigated in [29]. The authors are able to obtain good results with the use of the Streamline Upwind Petrov-Galerkin Method, which eliminates the spurious oscillations seen in results generated by traditional FEM and finite difference methods. In [46] the authors investigate crack initiation in the regions near localized heat sources, such as thermal shocks. The work most closely related to the present investigation is [31] in which a moving, localized spike in the internal source is analyzed using the X-FEM. The authors were able to efficiently solve the problem using special enrichment functions based on their knowledge of the solution. The model problem to be analyzed in this paper is obtained from [31] and used as a benchmark for the proposed methodology.

In the next section, we discuss the formulation of the governing equations, i.e. the steady-state heat equation. A brief presentation of generalized finite element (GFEM) approximations [1, 2, 15, 35, 42] is provided in Section 3. Section 4 provides a detailed account of the model problem to be investigated in this paper. Output obtained from standard FEA [37, 48] is presented along with data obtained from GFEM analyses of the same problem. Motivated by the potential to solve the problem using specially-designed, but more general shape functions, a detailed analysis of the model problem using the Generalized Finite Element Method with global-local enrichments ($GFEM^{\text{g-l}}$) is performed to study the methods ability to effectively control the error in the solution. The final section then provides the main conclusions and future directions for the current investigation.

2 Problem Formulation

This paper investigates steady-state heat transfer problems with solutions exhibiting highly localized sharp thermal gradients. Consider a domain $\Omega \subset \boldsymbol{R}^3$ with boundary $\partial\Omega$ decomposed as $\partial\Omega = \Gamma^u \cup \Gamma^f$ with $\Gamma^u \cap \Gamma^f = \emptyset$. The strong form of the governing equation is given by Poisson's equations

$$-\nabla(\boldsymbol{\kappa}\nabla u) = q(\boldsymbol{x}) \quad \text{in} \quad \Omega \tag{1}$$

where $u(\boldsymbol{x})$ is the temperature field, $\boldsymbol{\kappa}$ is the thermal conductivity tensor and $q(\boldsymbol{x})$ is the internal heat source. The following boundary conditions are prescribed on $\partial\Omega$

$$u = \bar{u} \quad \text{on} \quad \Gamma^u \tag{2}$$

$$-\boldsymbol{\kappa}\nabla u\cdot\boldsymbol{n}=\bar{f}\quad\text{on}\quad\Gamma^f \tag{3}$$

where $\boldsymbol{n}$ is the outward unit normal vector to Γ^f and $\bar{f}$ and $\bar{u}$ are prescribed normal heat flux and temperature, respectively.

3 Generalized FEM Approximations

The generalized FEM [1, 2, 15, 35, 42] is one instance of the partition of unity method. This method has its origins in the works of Babuška et al. [1, 2, 30] (under the names "special finite element methods", "generalized finite element method" and "finite element partition of unity method") and Duarte and Oden [12, 18, 19, 20, 35] (under the names "*hp* clouds" and "cloud-based *hp* finite element method"). Several meshfree methods proposed in recent years can also be viewed as special cases of the partition of unity method. In the GFEM, discretization spaces for a Galerkin method are defined using the concept of a partition of unity and local spaces that are built based on a-priori knowledge about the solution of a problem. A shape function, $\phi_{\alpha i}$, in the GFEM is computed from the product of a linear finite element shape function, φ_α, and an enrichment function, $L_{\alpha i}$,

$$\phi_{\alpha i}(\boldsymbol{x})=\varphi_\alpha(\boldsymbol{x})L_{\alpha i}(\boldsymbol{x})\qquad(\text{no summation on }\alpha), \tag{4}$$

where α is a node in the finite element mesh. Figure 1 illustrates the construction of GFEM shape functions. The linear finite element shape functions $\varphi_\alpha,\ \alpha=1,\ldots,N$, in a finite element mesh with N nodes constitute a partition of unity, i.e., $\sum_{\alpha=1}^{N}\varphi_\alpha(\boldsymbol{x})=1$ for all $\boldsymbol{x}$ in a domain Ω covered by the finite element mesh. This is a key property used in partition of unity methods. An a-priori error estimate for partition of unity approximations and, in particular, for the generalized finite element method, was proved by Babuška et al. [1, 2, 30].

Enrichment functions The GFEM has been successfully applied to the simulation of boundary layers [13], dynamic propagating fractures [16], line singularities [15], acoustic problems with high wave number [3], polycrystalline microstructures [40], porous materials [42], etc. All these applications have relied on closed form enrichment functions that are known to approximate well the physics of the problem. These custom or special enrichment functions are able to provide more accurate and robust simulations than the polynomial functions traditionally used in the standard FEM, while relaxing some meshing requirements of the FEM. However, for many classes of problems–like those involving multiscale phenomena or non-linearities–enrichment functions with good approximation properties are, in general, not available analytically. In Section 5, we present a procedure to numerically build enrichment functions for problems exhibiting highly localized sharp thermal gradients. The approach is based on the solution of local boundary value problems and can be used when no or limited a-priori knowledge about the solution is available.

4 Model Problem

A model problem representative of thermal loads experienced by a hypersonic vehicle subjected to a Type IV interaction (Cf. Section 1) is defined in this section. This problem is used to assess the performance of the FEM and the GFEM when solving problems with solutions exhibiting highly localized sharp thermal

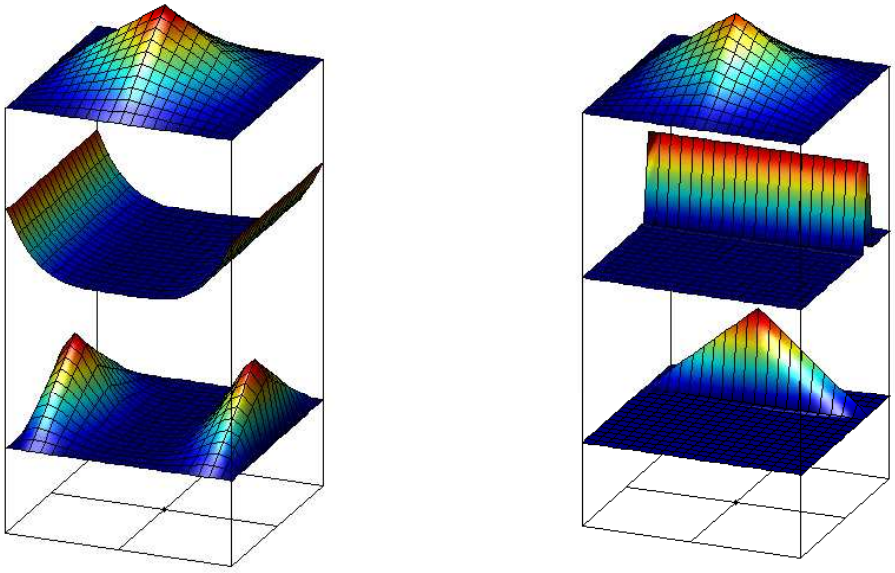

(a) (b)

Figure 1: Construction of a generalized FEM shape function using a polynomial (a) and a non-polynomial enrichment (b). Here, φ_α is the function at the top, the enrichment function, $L_{\alpha i}$, is the function in the middle, and the generalized FE shape function, $\phi_{\alpha i}$, is shown at the bottom.

gradients. The solution of the model problem is given by

$$u(x) = \exp^{-\gamma(x-x_0)^2} + \sin\left(\frac{\pi x}{L}\right) \tag{5}$$

where $x_0 = 125\,mm$, $L = 500, mm$ and γ is a parameter controlling the roughness of the solution. Unless otherwise indicated, the value of γ is taken as 1.0. The temperature profile (5) is shown in Figure 2. The temperature distribution on a plate Ω has a sharp localized spike in a small neighborhood of x_0, similar to the types of distributions described in [7, 47]. This model problem was originally proposed by Merle and Dolbow [31] and was also analyzed by O'Hara [36].

The domain is taken as $\Omega = \{\boldsymbol{x} \in \boldsymbol{R}^3 : 0 < x < 500,\ 0 < y < 250, 0 < z < 30\}$ where all dimensions are in *mm*. Homogeneous Dirichlet boundary conditions are applied on faces $x = 0$ and $x = 500$ and homogeneous Neumann boundary conditions are prescribed on all other faces. A heat source given by

$$q(\boldsymbol{x}) = -\nabla^2 u(x),$$

with u defined in (5), is prescribed in Ω.

The energy norm associated with the problem defined in Section 2 is given by

$$\|u\|_E = \sqrt{B(u,u)} = \sqrt{\int_\Omega (\nabla u)\boldsymbol{\kappa}(\nabla u)\, d\Omega}$$

where $B(u,u)$ is the bilinear form associated with the Laplace operator.

In the numerical experiments presented below, the accuracy of a numerical approximation u_h of u is mea-

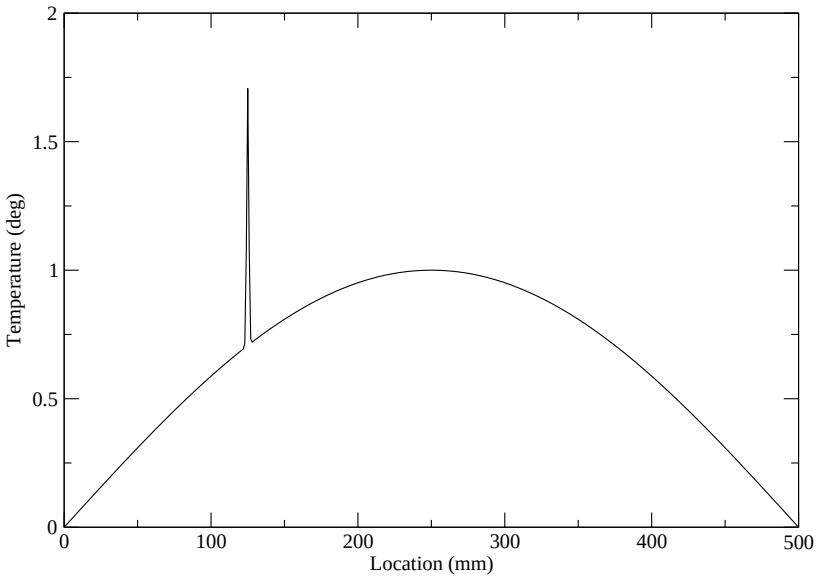

Figure 2: Temperature profile of model problem. The solution is smooth everywhere in the domain except in a small neighborhood of $x_0 = 125$ *mm*, where a sharp temperature spike develops.

sured using the relative error in the energy norm, i.e.,

$$e_E^r = \frac{\|u - u_h\|_E}{\|u\|_E} = \sqrt{\frac{B(u,u) - B(u_h,u_h)}{B(u,u)}}$$

The reference value for the energy of the solution (5) is taken as

$$B(u,u) = 9474.62$$

4.1 Convergence Analysis

In this section, the model problem described above is solved using the FEM and the GFEM. One, two and three-dimensional discretizations are used. This is possible due to the one-dimensional nature of the exact solution. In all the numerical experiments presented below, a high order Gaussian quadrature rule was used to compute the load vector over elements near the thermal spike at x_0. This is required due to the non-polynomial nature of heat source q. In the case of three-dimensional discretizations, a tensor-product Gaussian rule with 729 points is used. This rule was selected such that the convergence studies presented below are not affected by integration errors. Details on the numerical experiments used in the selection of this rule can be found in [36].

For 1-D analyses, the domain is a 1-dimensional bar, 500 *mm* in length, discretized with either 2-node *p*-hierarchical elements, or 2-node GFEM elements. Figure 3 shows how the 1-D meshes are broken up into three regions. The left- and right-most regions have fixed element sizes h_L and h_R, respectively. The middle region, containing the spike (120 $mm \leq x \leq$ 130 *mm*), is the only region which is refined, with element size h_i. For 2-D analyses, the domain is 500 *mm* in length, 2 *mm* in width, and discretized with 8-node (quadratic) or 4-node (linear) quadrilateral elements. Uniform meshes are used in the 2-dimensional case. For the 3-D analyses, the domain is discretized using 4-node GFEM tetrahedral elements. In the 3-dimensional case the mesh is again locally refined, as shown in Figure 4, where refinement is done only in the portion of

the domain which contains the peak. The element size in corresponding plots refers to the length in the x-direction of the smallest elements in the refined region.

Figure 3: Typical structure of the locally refined meshes used in the 1-D model. Element size in subsequent plots refers to h_i.

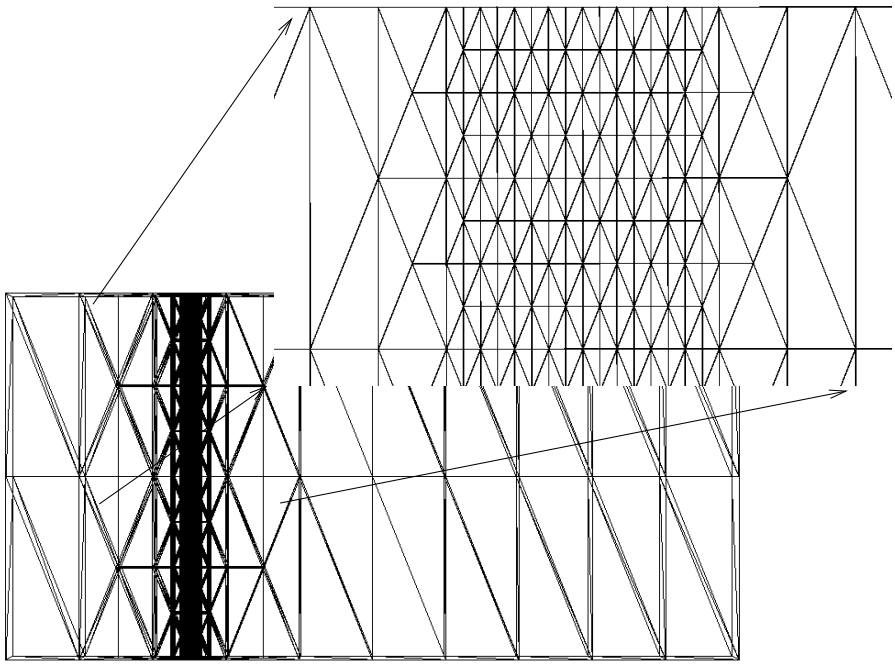

Figure 4: Locally refined 3-D mesh using a bounding box to define the region of local mesh refinement.

Convergence in energy norm of one dimensional FEM and GFEM discretizations is shown Figure 5. Linear and quadratic p-hierarchical FEM [43] and two-node quadratic GFEM [15, 35] elements are used. The convergence rates are denoted in the plot as $'B'$. From the plot, we can observe that quadratic GFEM and p-hierarchical FEM deliver the same level of accuracy. Thus, the curves for these elements coincide. The curves also show that there is a delay in reaching the optimal rate of convergence due to the rough nature of the solution, and the difficulty in resolving the localized thermal spike. The asymptotic convergence rates obtained are very close to the optimal rates of 1.0 for linear elements (B = 0.97), and 2.0 for quadratic elements (B = 1.96).

Figure 6 shows convergence in energy norm for quadratic discretizations with 1-D and 3-D GFEM elements; 1-D p-hierarchical elements; and 2-D Serendipity elements. The relative error in energy norm is plotted against element size in the x-direction. The convergence behavior is similar in each of the four discretization sequences used, achieving near the theoretical convergence rate of 2.0 (B = 1.96).

Figure 7 shows the convergence in energy norm of 3-D GFEM discretizations. The data for the quadratic element is the same as in Figure 6, but here the relative error in energy norm is plotted versus the number of degrees of freedom instead of element size. It is quite apparent that in 3-D, the required element size to achieve acceptable error values translates into a very large number of degrees of freedom. In the case of

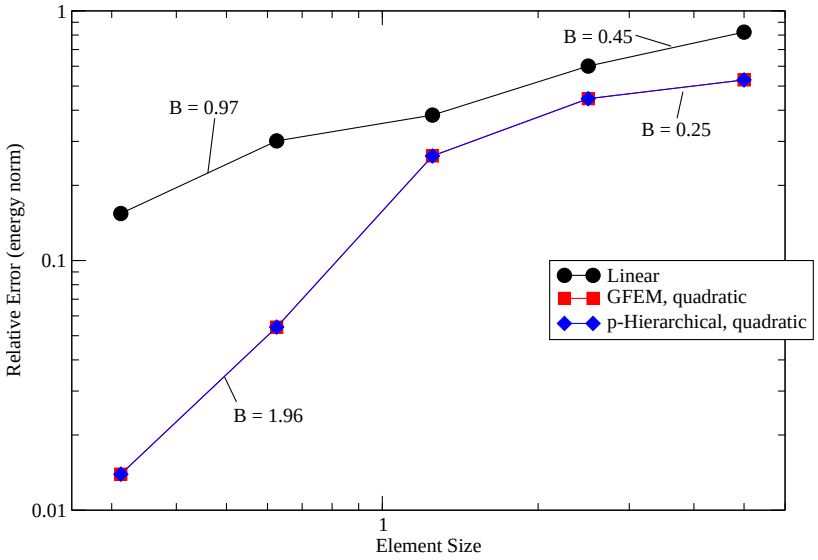

Figure 5: Convergence in energy norm for low order 1-D generalized and *p*-hierarchical finite elements. Quadratic GFEM and *p*-hierarchical FEM deliver the same level of accuracy. Thus, only two curves can be seen in the plot.

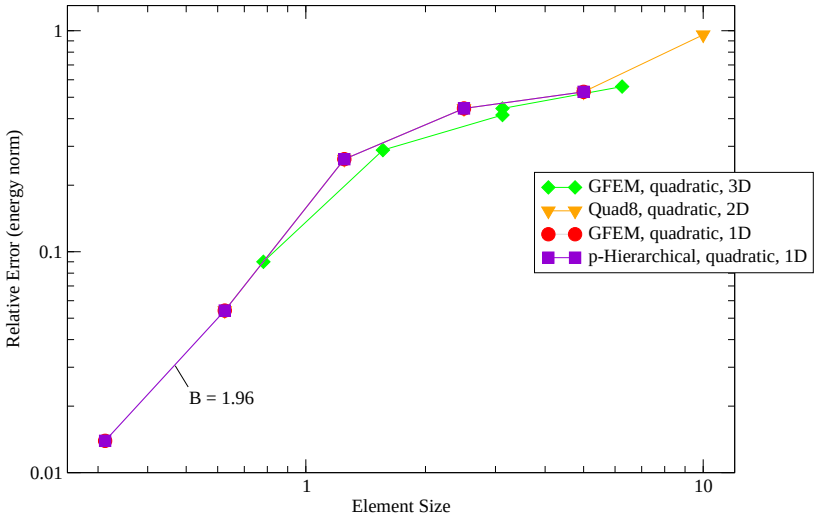

Figure 6: Convergence in energy norm for discretizations with 1-D and 3-D GFEM elements; 1-D *p*-hierarchical elements; and 2-D quadratic Serendipity elements. The curves for 1-D elements coincide.

linear elements, nearly 10^6 degrees of freedom were required to achieve an error level below 10 %. With this in mind, and considering that the geometry of the domains we are interested are much more complex than in our model problem and that time dependent effects must be considered, a more efficient solution methodology is required. One point to take note of is that in Figure 7, the relative error values are cut off at 1.0. As can be seen in the plot, there is a pre-convergent zone, where the error is 100 percent or higher, before a minimal level of refinement is reached. The pre-convergent regions on the curves are due to the mesh being too coarse to capture the localized behavior of the solution. A similar phenomenon is observed in [26] in which the capability of the finite element method to solve Helmholtz's equation is investigated.

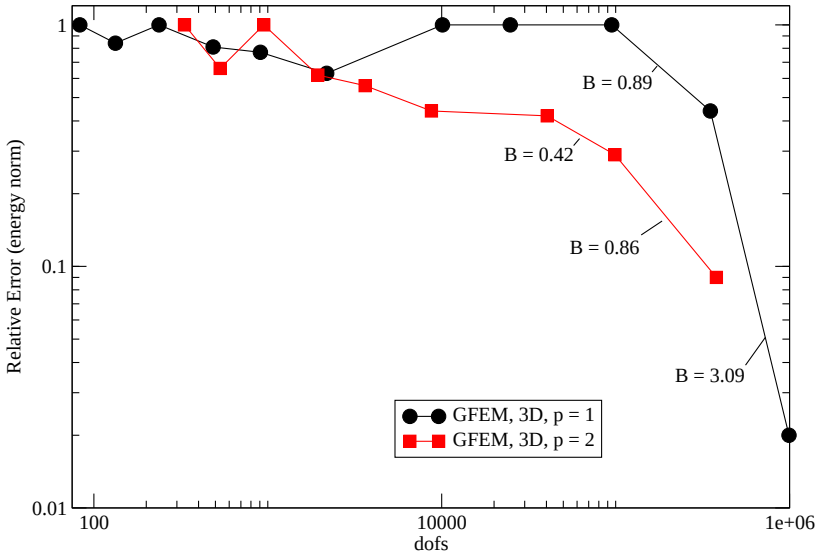

Figure 7: Convergence in energy norm for 3-D linear and quadratic tetrahedral elements. Sequences of meshes locally refined around the thermal spike are used.

4.1.1 Thermal gradient not aligned with mesh

In all the discretizations used previously, the spike in the loading was favorably oriented with respect to the mesh. In the previous analysis, there were element edges oriented in the global x-direction which coincides with the direction of the gradient in the temperature profile shown in Figure 2. This may not always be the case in practice, however; because the orientation of shock waves and thermal loadings may not line up with a primary axis of the coordinate system used to create the mesh or if an unstructured mesh is used. The effect of the orientation of the elements with respect to the gradient in the temperature profile is investigated in this section.

The model problem with roughness parameter $\gamma = 0.05$ is solved on domains with different orientations with respect to the gradient in the temperature profile. In the first case, the domain is as defined in Section 4 while in the second one the domain is rotated 45 degrees clockwise. In this case, the line along the thermal spike cuts the elements at a 45 degree angle. Figure 8 shows one mesh with this orientation. Neumann boundary conditions derived from the analytic solution (5) are applied to all faces of this domain. Quadratic tetrahedral GFEM elements are used in both cases. The reference value for the exact strain energy for the case of the domain oriented as in the previous section is taken as $B(u,u) = 2179.21$. In the second case, the reference value is taken as $B(u,u) = 2992.80$, and was obtained using a mesh with 23 levels of local refinement.

Figure 9 shows the convergence in the energy norm for the two domain orientations considered. From this

plot it can be seen that a significant increase in the number of degrees of freedom, in some instances up to 100 times more, is required to solve for the situation when the peak does not line up with the mesh, and in fact with this situation there is a pre-convergent zone which does not show up for the case where the peak is aligned with the mesh. While we are not solving the same problem in both cases, the smoothness of the solution is the same. Thus it is reasonable to attest that the difference in convergence between the two cases is mainly due to the change of orientation of the thermal layer with respect to the mesh.

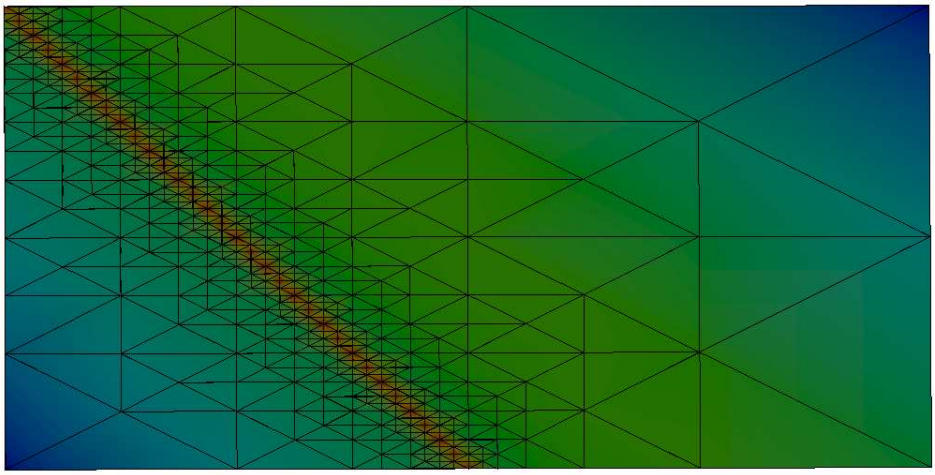

Figure 8: Temperature distribution computed on a mesh where the line along the thermal peak cuts the domain at a 45 degree angle. Roughness parameter $\gamma = 0.05$.

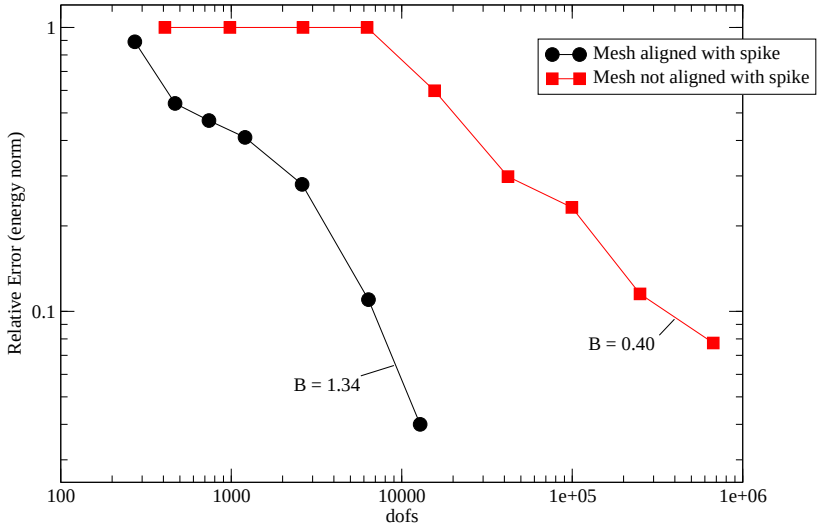

Figure 9: convergence in the energy norm for the two domain orientations considered. In one case, the internal layer is aligned with element edges while in the second case it is not. The roughness parameter γ is taken as 0.05.

From the numerical experiments presented above, it is clear that the approximation of functions exhibiting highly localized gradients requires strongly refined meshes. High order elements can reduce the need for mesh refinement but not eliminate it [36]. *Hp* discretizations in which both element size and polynomial order are optimally distributed in the domain [8, 9, 10, 34, 38, 39] are able to deliver exponential convergence

for problems like the one analyzed here. Optimal *hp* discretizations use strongly refined meshes around regions with sharp thermal gradients. This creates some difficulties in the case of, e.g., time-dependent problems. The refinement/unrefinement must follow a moving internal layer and thus the problem must be solved from scratch after each mesh update even in the case of linear problems. In the next sections, we investigate the possibility of exploring the flexibility provided by the generalized FEM to avoid mesh refinement/unrefinement cycles and instead using customized enrichment functions able to approximate well the behavior of the solution on a fixed coarse mesh. Avoiding mesh refinement/unrefinement will be important in the consideration of transient problems due to the energy conserving nature of avoiding the re-meshing process, as proven in [6].

4.2 GFEM with Special Enrichment Functions

In all numerical experiments presented in previous sections, only polynomial enrichment functions are used. As a result, a high level of mesh refinement is required in order for acceptable error levels to be obtained. Merle and Dolbow [31], demonstrated that far greater efficiency can be achieved when a-priori knowledge of the solution is used, and an exponential enrichment function of the form

$$L(x) = \exp^{-(x-x_0)^2} \tag{6}$$

is used to create GFEM shape functions specifically tailored to solve the model problem previously described.

For the purpose of comparison, a one-dimensional mesh consisting of five, equally-sized, quadratic GFEM elements and 12 degrees of freedom was used to solve the model problem, yielding a relative error in the energy norm of 0.996. When the element containing the thermal spike is enriched with the exponential enrichment function (6) the relative error in the energy norm drops to $1.58x10^{-3}$, a three-orders of magnitude reduction by adding two degrees of freedom to the discretization. Figure 10 shows the solution obtained with this discretization.

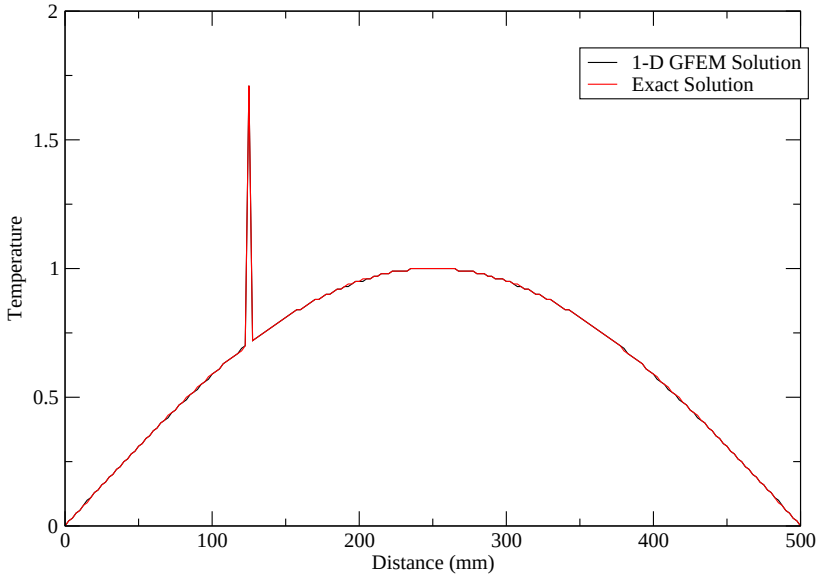

Figure 10: One-Dimensional GFEM solution computed on a uniform mesh with five quadratic elements. The element containing the thermal spike is enriched with exponential enrichment function (6).

This numerical experiment demonstrates that it is possible to achieve a high level of accuracy using coarse meshes *provided appropriate enrichment functions are used.* Nonetheless, enrichments able to approximate well small scale behavior like the one exhibited in our model problem are, in general, not known. Thus, a more general approach to building special enrichment functions is needed. The proposed approach is based on the generalized finite element method with global-local enrichments (*GFEM*$^{\text{g-l}}$) presented in [14, 17]. As demonstrated in the next sections, the so-called global-local enrichments can be defined even when limited or no a-priori information about the solution of a problem is available while enabling the use of coarse macro-scale meshes.

5 Generalized Finite Element Analysis with Global-Local Enrichments

In this section, we present a procedure to build enrichment functions for the class of problems governed by (1) and subjected to boundary conditions (2) and (3). The formulation and application of the *GFEM*$^{\text{g-l}}$ to three-dimensional elasticity equations can be found in [14, 17, 28]

5.1 Formulation of Global Problem

Consider a domain $\bar{\Omega}_G = \Omega_G \cap \partial\Omega_G$ as illustrated in Figure 11(a). The boundary is decomposed as $\partial\Omega_G = \Gamma_G^u \cup \Gamma_G^f$ with $\Gamma_G^u \cap \Gamma_G^f = \emptyset$. The solution u of the global or macroscale problem obeys Poisson's equation (1) on Ω_G and the boundary conditions prescribed on $\partial\Omega_G$ and given by (2) and (3). A generalized FEM approximation, u_G^0, of the solution u can be found solving the following problem:

Find $u_G^0 \in X_G^{hp}(\Omega_G) \subset H^1(\Omega_G)$ such that, $\forall\, v_G^0 \in X_G^{hp}(\Omega_G)$

$$\int_{\Omega_G} \nabla u_G^0 \boldsymbol{\kappa} \nabla v_G^0 d\Omega + \eta \int_{\Gamma_G^u} u_G^0 v_G^0 d\Gamma = \int_{\Omega_G} q v_G^0 d\Omega + \int_{\Gamma_G^f} \bar{f} v_G^0 d\Gamma + \eta \int_{\Gamma_G^u} \bar{u} v_G^0 d\Gamma \tag{7}$$

where, $X_G^{hp}(\Omega_G)$ is a discretization of $H^1(\Omega_G)$ built with generalized FEM shape functions, and η is a penalty parameter. The enforcement of the Dirichlet boundary condition could also be done using, e.g., the Nitsche method or the Characteristic function method. Details on these methods, as well as their theoretical analysis within the framework of the GFEM, are presented in the survey paper by Babuska et al. [4]. In this paper, the penalty method is used due to its simplicity of implementation.

Problem (7) leads to a system of linear equations for the unknown degrees of freedom of u_G^0. The mesh used to solve problem (7) is typically a coarse quasi-uniform mesh. This global or macroscale problem (7) is denoted hereafter as *initial global problem* for convenience.

5.2 Local Problems

Let Ω_{loc} denote a subdomain of Ω_G as illustrated in Figure 11(b). In this paper, we consider the case in which the solution u exhibits a strong internal layer, in the form of a sharp spike, in the local domain Ω_{loc}.

The following local problem is solved on Ω_{loc} after the global solution u_G^0 is computed as described above:

Find $u_{loc} \in X_{loc}^{hp}(\Omega_{loc}) \subset H^1(\Omega_{loc})$ such that, $\forall\, v_{loc} \in X_{loc}^{hp}(\Omega_{loc})$

$$\begin{aligned}
&\int_{\Omega_{loc}} \nabla u_{loc} \boldsymbol{\kappa} \nabla v_{loc} d\Omega + \eta \int_{\partial\Omega_{loc} \setminus (\partial\Omega_{loc} \cap \Gamma_G^f)} u_{loc} v_{loc} d\Gamma = \\
&\eta \int_{\partial\Omega_{loc} \setminus (\partial\Omega_{loc} \cap \partial\Omega_G)} u_G^0 v_{loc} d\Gamma + \eta \int_{\partial\Omega_{loc} \cap \Gamma_G^u} \bar{u} v_{loc} d\Gamma + \int_{\Omega_{loc}} q v_{loc} d\Omega + \int_{\partial\Omega_{loc} \cap \Gamma_G^f} \bar{f} v_{loc} d\Gamma
\end{aligned} \tag{8}$$

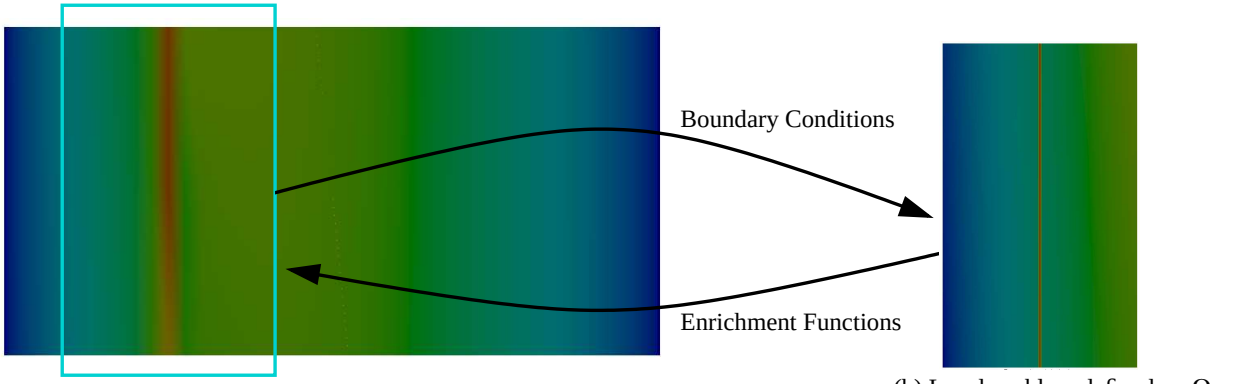

(a) Global problem defined on Ω_G.

(b) Local problem defined on Ω_{loc}.

Figure 11: The generalized FEM with global-local enrichment functions. (a) Initial and enriched global problems discretized with a coarse mesh. The initial global problem provides boundary conditions for local problems containing sharp thermal spikes. (b) Local problem used to compute global-local enrichment functions.

where, $X_{loc}^{hp}(\Omega_{loc})$ is a discretization of $H^1(\Omega_{loc})$ using GFEM shape functions.

A key aspect of problem (8) is the use of the generalized FEM solution of the global problem, u_G^0, as boundary condition on $\partial\Omega_{loc}\backslash(\partial\Omega_{loc}\cap\partial\Omega_G)$. Exact boundary conditions are prescribed on portions of $\partial\Omega_{loc}$ that intersect either Γ_G^u or Γ_G^f. Problem (8) is named hereafter *local problem* for convenience.

5.3 Global-Local Enrichment Functions

The procedure described above to compute the local solution u_{loc} is the well known global-local analysis [11, 21, 33]. This procedure enables the computation of local quantities of interest while not requiring modifications on the usually large and complex global mesh. It is also computationally efficient since a single global analysis needs to be performed, even when local quantities must be computed at several subdomains $\Omega_{loc}\subset\Omega_G$. However, the error of the local solution, u_{loc}, depends not only on the discretization used in local domain Ω_{loc}, but also on the quality of boundary conditions used on $\partial\Omega_{loc}\backslash(\partial\Omega_{loc}\cap\partial\Omega_G)$, which are provided by the global solution u_G^0. One approach to address the poor accuracy of these boundary conditions is to use a sufficiently large local domain. Nonetheless, the minimum size of Ω_{loc} for acceptable results is problem dependent. In particular, for the class of problems we are interested, the error of the global solution u_G^0 may be large even far from the thermal spike. This is illustrated in Figure 12. Thus, the local solution u_{loc} will have in general a large error, even when very fine meshes are used in the local domain.

In the GFEM with global-local enrichments ($GFEM^{\text{g-l}}$) the poor accuracy of u_{loc} is addressed by going one step further in the analysis and using u_{loc} as an enrichment function for the global discretization. Generalized FEM shape functions for the global problem are defined as

$$\phi_\alpha = \varphi_\alpha u_{loc} \tag{9}$$

where φ_α denotes a partition of unity function of the coarse global mesh and u_{loc} is called a *global-local enrichment function*. The function defined in (9) is used at nodes $\boldsymbol{x}_\alpha$ of the global mesh whose support, ω_α, is contained in the local domain Ω_{loc}. The global problem enriched with these functions is solved and quantities of interest computed. The solution of this *enriched global problem* is hereafter denoted by u_G^E. The $GFEM^{\text{g-l}}$ approach is illustrated in Figure 11. The global solution provides boundary conditions for local problems while local solutions are used as enrichment functions for the global problem through the

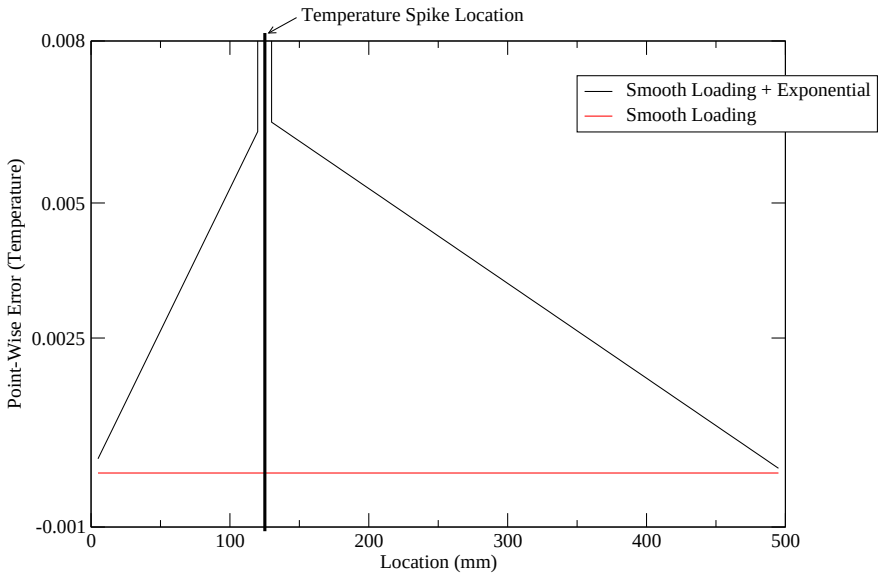

Figure 12: Error of solution computed on a uniform global mesh with 50 elements in the $x-$direction and one element in the $y-$ direction. Standard eight-node quadratic finite elements are used. The location of the thermal spike is indicated in the figure. We can observe that the error in the computed temperature is relatively large even far from the thermal spike. Error when the exact solution is given by $u(\boldsymbol{x}) = \sin(\pi x/L)$, i.e., the thermal spike $e^{-\gamma(x-x_0)^2}$ is removed is also provided. In this case, the error of the finite element solution is very small.

partition of unity framework of the GFEM. The procedure described above may be repeated. The solution u_G^E is used as boundary conditions for the local problem and so on. This strategy is investigated in Section 6.2.

The enriched global problems do not have, in general, to be solved from scratch since the shape function (9) is hierarchically added to the global space and only a small number of nodes in the global problem is enriched. This is demonstrated in [14]. The relation of the *GFEM*$^{\text{g-l}}$ with other methods is also discussed in [14].

The performance of the *GFEM*$^{\text{g-l}}$ when solving steady-state heat transfer problems with solutions exhibiting highly localized sharp thermal gradients is investigated in the next sections.

6 Analysis of Model Problem Using the *GFEM*$^{\text{g-l}}$

The generalized FEM with global-local enrichment functions (*GFEM*$^{\text{g-l}}$) described above is used in this section to solve the model problem defined in Section 4. The global, Ω_G, and local, Ω_{loc}, domains are discretized with four node tetrahedral GFEM elements [15]. Quadratic and quartic ($p = 4$) elements are used in global and local domains, respectively. Uniform meshes in x-, y- and z-direction are used in the global domain. The meshes are created by first generating a mesh of hexahedral elements and then dividing each element into 6 tetrahedral elements. Hereafter, meshes are defined based on the number of hexahedral elements used in their generation, not the number of tetrahedral elements. Each global mesh has 2 elements in the y-direction, and 1 element in the z-direction. Mesh 0x has 10 elements in the x-direction, Mesh 1x has 20 element in the x-direction, and Mesh 2x has 40 elements in the x-direction. The global domains show increasing levels of refinement in the x-direction only because the solution only exhibits a gradient

in the $x-$direction, and is constant in y and z. These meshes are shown in Figures 18(c), 19(c) and 20(c), respectively.

Creation of Local Problems Local domains and their corresponding initial discretizations are defined by copying elements from the global mesh around the thermal spike. This is done with the aid of global seed nodes which are selected via a bounding box containing the temperature spike. For the analyses presented here, the same bounding box is used for each of the three global meshes–Meshes 0x, 1x and 2x. As such, the smallest possible bounding box size is determined by the coarsest global mesh, Mesh 0x. The bounding box is defined from $\min = [100, 0, 0]$ to $\max = [150, 250, 30]$. Figure 13 illustrates this procedure. Let $\mathscr{I}_{seed}$

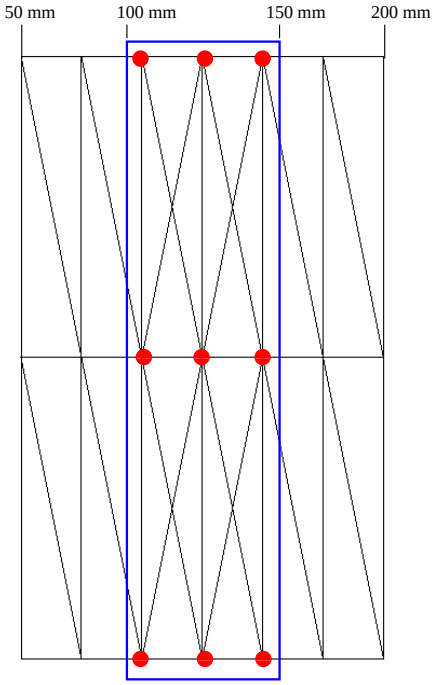

Figure 13: Extraction of initial local mesh from global Mesh 1x. The bounding box used for selection of seed nodes is shown (rectangle) along with the seed nodes (solid circles). Nine seed nodes are shown, but there are eighteen in total: Nine on top surface (shown) and nine on the bottom surface of mesh.

denote the indices of all global seed nodes in the bounding box. A local domain corresponding to a mesh with one layer of elements around the seed nodes is given by

$$\Omega_{loc}^{nlay=1} := \bigcup_{\beta \in \mathscr{I}_{seed}} \omega_\beta$$

where ω_β is the union of (copy of) global elements sharing node $\boldsymbol{x}_\beta$, $\beta \in \mathscr{I}_{seed}$. Local domains with additional layers of elements around the seed nodes are defined analogously. The mesh corresponding to a local domain with m layers of elements around a given set $\mathscr{I}_{seed}$ is given by the union of (copy of) the mesh with $m-1$ layers and the global elements sharing a vertex node in the mesh with $m-1$ layers.

The size of the local domains are also kept constant for each global mesh used, and once again are determined by Mesh 0x. One layer of elements in Mesh 0x is selected, resulting in the local domain $\Omega_{loc} = \{\boldsymbol{x} \in \boldsymbol{R}^3 : 50 < x < 200,\ 0 < y < 250, 0 < z < 30\}$. Two and four layers of elements around the seed nodes are used for Meshes 1x and 2x, respectively. Again, this was selected to maintain a constant size in the local

domain.

The local meshes themselves are then refined by bisecting all tetrahedral elements inside of the bounding box defined by $\min = [122.5, 0, 0]$ and $\max = [127.5, 250, 30]$ for the case when $\gamma = 1.0$. A local mesh is shown in Figure 14 corresponding to Mesh 1x with 9 levels of local refinement.

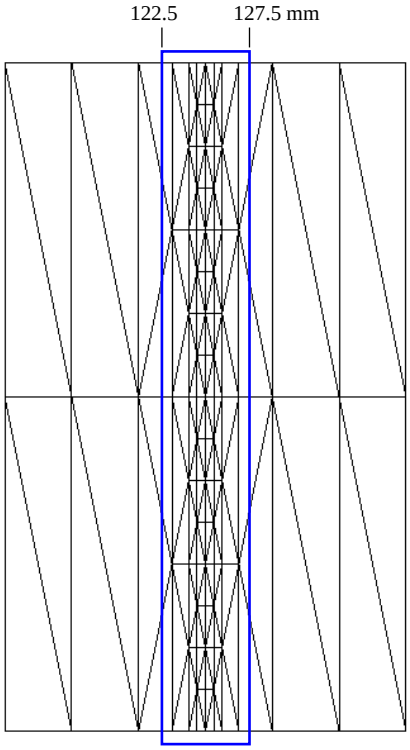

Figure 14: Local mesh extracted from Mesh 1x, and 9 levels of local refinement are used. The rectangle in the figure represents the bounding box used for refinement. (Not to scale)

The seed nodes used to create the local domains are the same nodes which are then enriched with the local solution (global-local enrichments). Twelve nodes are enriched on Mesh 0x; eighteen nodes are enriched on Mesh 1x and thirty nodes are enriched on Mesh 2x. This is illustrated in Figures 18(c), 19(c) and 20(c).

The number of degrees of freedom (DOFs) in the global problem remains almost constant when global-local enrichments are used. In addition, the number of DOFs in the enriched global problem does not depend on the number of DOFs in the local problem. Therefore, the number of DOFs in the enriched global problem is not a good measure for the computational cost of u_G^E. In the convergence analyses presented hereafter, the computational cost for both local and global problems are measured with respect to CPU time, not number of DOFs. All measures are in seconds. For plots dealing with local problems, the CPU time considers the time taken for assembly and solution of the local problem. Plots dealing with the enriched global domain consider the CPU time taken for assembly and solution of the enriched global domain as well as the assembly and solution time taken in the corresponding local domain. The CPU times are meant to reflect the total computational effort required to generate the solution of interest, which is the underlying reason for the selection of each component considered in each case.

6.1 *H*-extensions in the local problem

The convergence of the enriched global problem when *h*-extensions are performed in the local problem is investigated in this section. The local problems are solved using Dirichlet boundary conditions on $\partial\Omega_{loc}\backslash(\partial\Omega_{loc}\cap\partial\Omega_G)$ provided by the initial global problem as discussed in Section 5.2. For reasons which will become more clear in the subsequent sections, the methodology used in this section will be referred to as *Initial Global Problem with Spike*, or *IGw/S*.

Figure 15 shows the relative error in energy norm in the enriched global problems associated with meshes 0x, 1x and 2x. All three cases show convergence of the enriched global problem as the local problems are refined. The global mesh is kept fixed for each curve shown, only the global-local enrichments (solution of local problems) are updated. The CPU time on the horizontal axis includes the CPU time taken for assembly and solution of the enriched global domain as well as the assembly and solution time taken in the corresponding local domain. Thus, as the local domains are refined, the reported CPU time increases. From the figure, we can observe that the pre-asymptotic range reduces as finer global meshes are used. In addition, for a given computational effort the accuracy of the enriched global solution computed on Mesh 2x can be up to one order of magnitude higher than on the other two meshes.

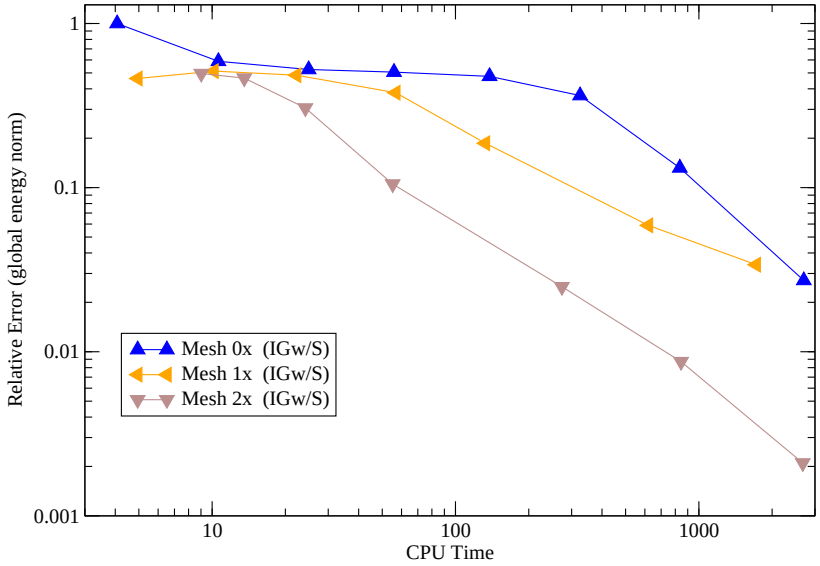

Figure 15: Relative error in energy norm for enriched global problems associated with meshes 0x, 1x and 2x. Each curve corresponds to a fixed global mesh and *h*-extensions in the local problems. The CPU time includes the CPU time taken for assembly and solution of the enriched global domain as well as the assembly and solution time taken in the corresponding local domain.

Figure 16 shows the relative error in energy norm in the local problems subjected to boundary conditions provided by global solutions computed on meshes 0x, 1x and 2x. Very large errors and poor or no convergence can be observed. Local problems subjected to boundary conditions from global meshes 1x and 2x initially show convergence but then the error levels off. This shows that the poor quality of the boundary conditions is controlling the error. This is confirmed in Sections 6.2 and 6.3 where we present two approaches to improve the quality of the boundary conditions for the local problems. Interestingly, the global problems enriched with these poor local solutions show convergence as discussed above, attesting the robustness of the proposed $GFEM^{g\text{-}l}$. However, the convergence of the enriched global problem will at some point level off since the local solutions do not converge to the solution of the global problem due to errors in boundary conditions applied to local problems. This can be observed in Figure 17 which shows more data points than

in Figure 15. The convergence for Meshes 1x and 2x level off due to poor quality of local solutions. The convergence for other meshes are also expected to eventually level off. In Sections 6.2 and 6.3 we propose two approaches to extend the convergent range of the enriched global problem.

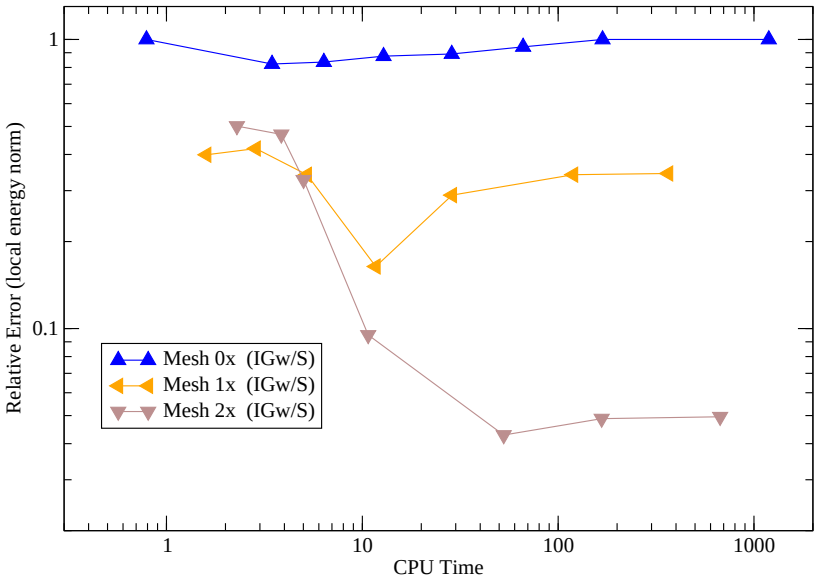

Figure 16: Relative error in energy norm for local problems subjected to boundary conditions provided by global solutions computed on meshes 0x, 1x and 2x. The CPU time considers the time taken for assembly and solution of the local problem.

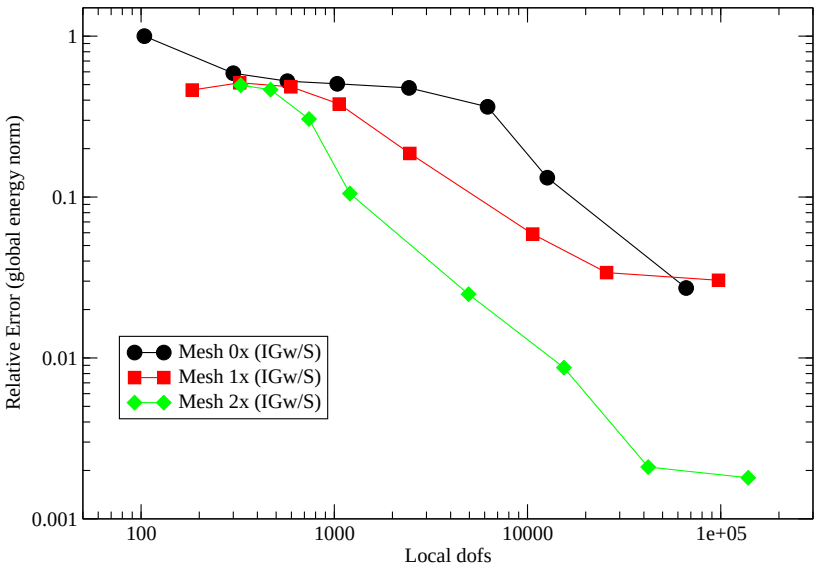

Figure 17: Data of Figure 15 plotted against the number of DOFs in the local problems. The plot includes data points that could not be included in Figure 15 due to a limitation of the function we use to measure CPU time.

Figures 18, 19 and 20 show temperature distributions computed in each phase of the *GFEM*$^{g\text{-}l}$–initial global, local, and enriched global problems–corresponding to global meshes 0x, 1x and 2x, respectively, and 13 levels of refinement in the local problems. Solutions of initial global problems solved with meshes 0x and

1x completely miss the thermal spike and as a result the local solutions are of poor quality. The thermal spike, however, is clearly captured in all three enriched global problems, attesting the importance of the extra step in the proposed *GFEM*$^{g\text{-}l}$. This is in agreement with the convergence plots shown in Figures 15 and 16. One other point of interest is the resolution of the spike in Figure 18(c) where a well-resolved spike can be seen in the temperature field even with the use of very large elements. In fact, the spike in the temperature field falls within elements, and not along a line of nodes, reflecting the shape of the specially-tailored enrichment functions from the local problem.

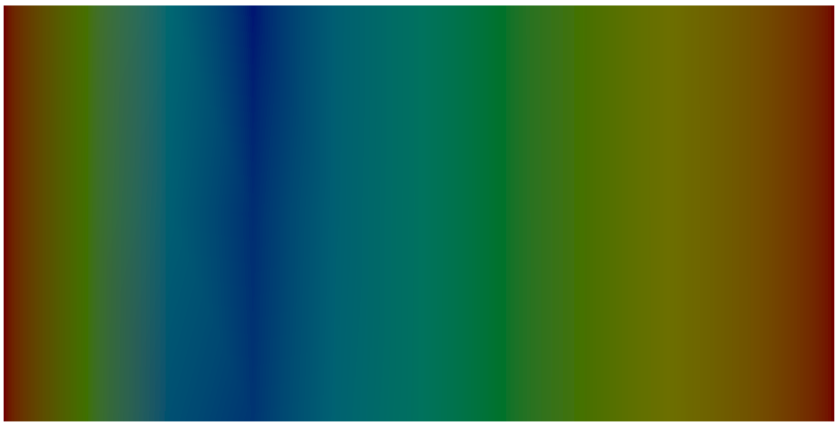

(a) Solution of initial global problem.

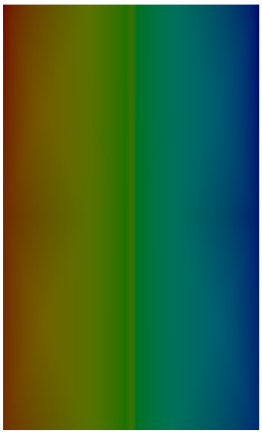

(b) Solution of local problem.

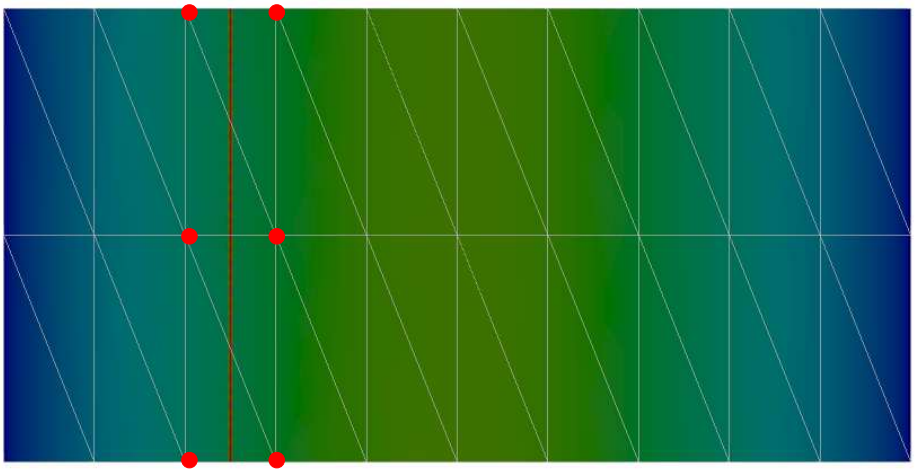

(c) Solution of enriched global problem.

Figure 18: Temperature distributions computed in the initial global, local, and enriched global problems corresponding to global Mesh 0x and 13 levels of refinement in the local problem. The *IGw/S* methodology is used. The thermal spike is well resolved in the enriched global problem even though it falls within quite large elements. Enriched nodes in global domain are denoted in Figure 18(c) by red glyphs.

(a) Solution initial global problem.

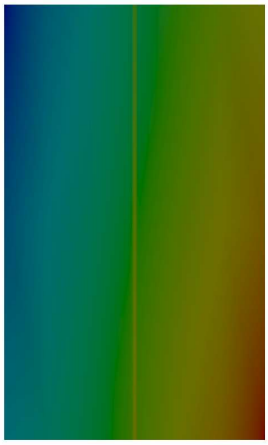

(b) Solution of of local problem.

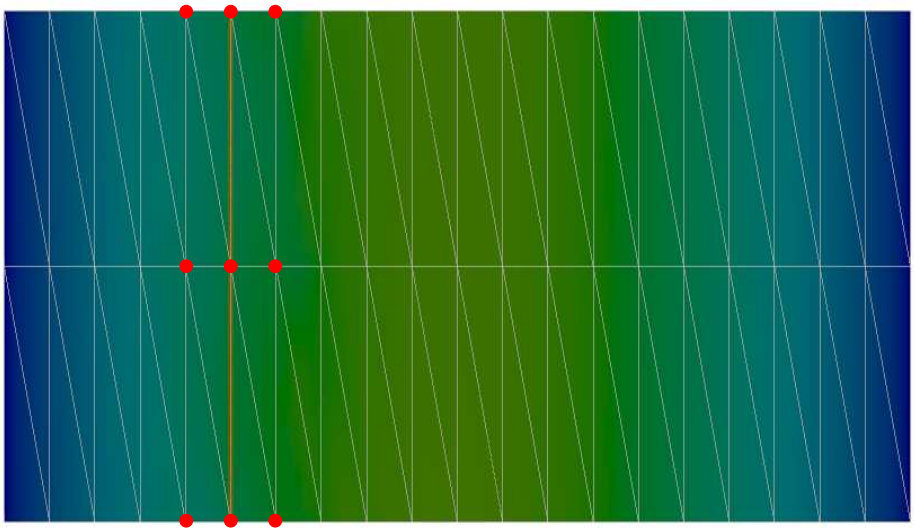

(c) Solution of enriched global problem.

Figure 19: Temperature distributions computed in the initial global, local, and enriched global problems corresponding to global Mesh 1x and 13 levels of refinement in the local problem. The *IGw/S* methodology is used. Enriched nodes in global domain are denoted in Figure 19(c) by red glyphs .

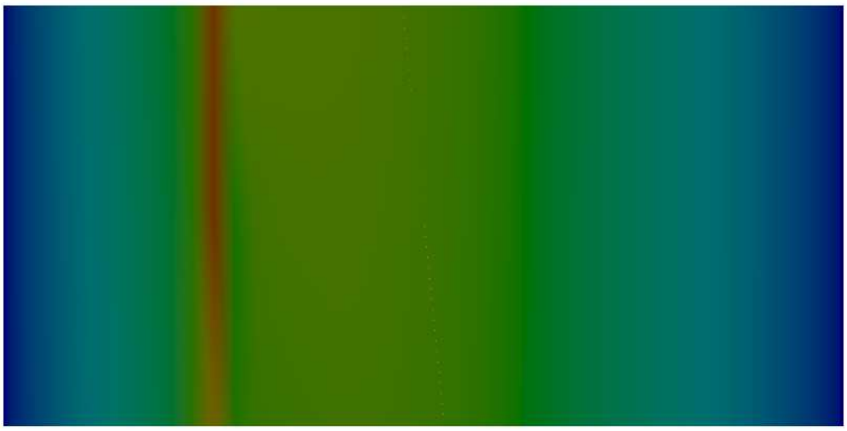

(a) Solution of initial global problem.

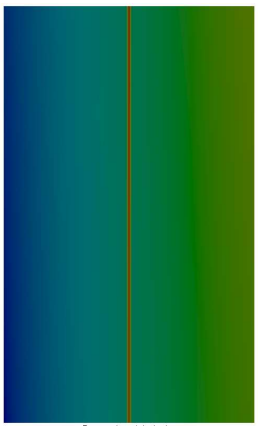

(b) Solution of local problem.

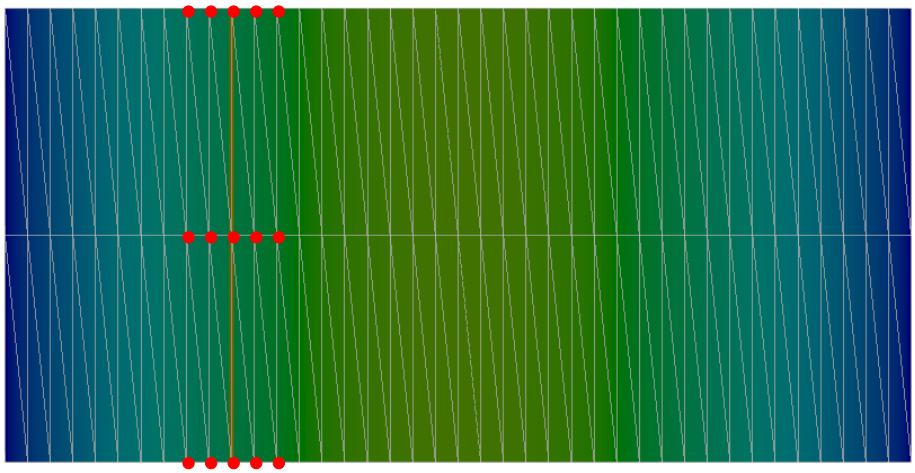

(c) Solution of enriched global problem.

Figure 20: Temperature distributions computed in the initial global, local, and enriched global problems corresponding to global Mesh 2x and 13 levels of refinement in the local problem. The *IGw/S* methodology is used. Enriched nodes in global domain are denoted in Figure 20(c) by red glyphs.

6.2 A Two-Step Approach to Improve Local Solutions

As discussed in Section 5.3, the error of the global solution u_G^0 may be large even far from the thermal spike (Cf. Figure 12). Thus, local problems may be subjected, for the class of problems we are interested, to poor boundary conditions. As a result, the error of the local solutions can not be controlled simply by mesh refinement or element enrichment (Cf. Figure 16). In this section, we address this issue by performing one additional global-local cycle. The solution u_G^E is used as boundary conditions for the local problems and then we proceed as before–Solve the local problems and enrich the global discretization with local solutions. For simplicity this approach is hereafter referred to as *IGw/S-II*–the two-step version of *IGw/S*. This particular approach is investigated because it has potential to be exploited in a transient solution to a time-dependent problem when the enriched global solution from time step t_n can be used as boundary conditions for the local problem at time step t_{n+1}.

Figure 21 shows the temperature distributions computed in the initial global, local, and enriched global problems of the *IGw/S-II* strategy. Here, the initial global problem corresponds to the enriched global problem in the *IGw/S* strategy. The thermal spike is well resolved in this problem and thus improved BCs are imposed on the local problem which can also capture well this behavior and, in turn, provide good enrichment functions for the enriched global problem (Cf. Figure 21(c)).

Figure 22 shows the relative error in energy norm in the local problems in strategies *IGw/S* and *IGw/S-II*. Local boundary conditions are provided by global solutions computed on meshes 0x, 1x and 2x. We can observe a dramatic difference between the two strategies. As expected, the local problems in the second step of the *IGw/S-II* strategy are subjected to much improved boundary conditions than in the first step which lead to the improvement seen in convergence.

Figures 23 shows the relative error in energy norm for enriched global problems in strategies *IGw/S* and *IGw/S-II*. All three cases, Meshes 0x, 1x and 2x, show convergence of the enriched global problem as the local problems are refined. The behavior of the energy norm is not as dramatically different between the two strategies, which is evidence of the robustness of the *GFEM*$^{\text{g-l}}$ to take local solutions which may be very poor and still deliver reasonable convergence in global domain. Nonetheless, some differences do exist at low error levels. The enriched global solution in strategy *IGw/S-II* does not level off as in the *IGw/S* strategy. Thus, the *IGw/S-II* strategy extends the range of target error level for the enriched global problem. Of course the convergence of the enriched global *IGw/S-II* may eventually level off but at a lower error level than in the *IGw/S* strategy. We have not, however, experienced this in any numerical experiments we have performed so far.

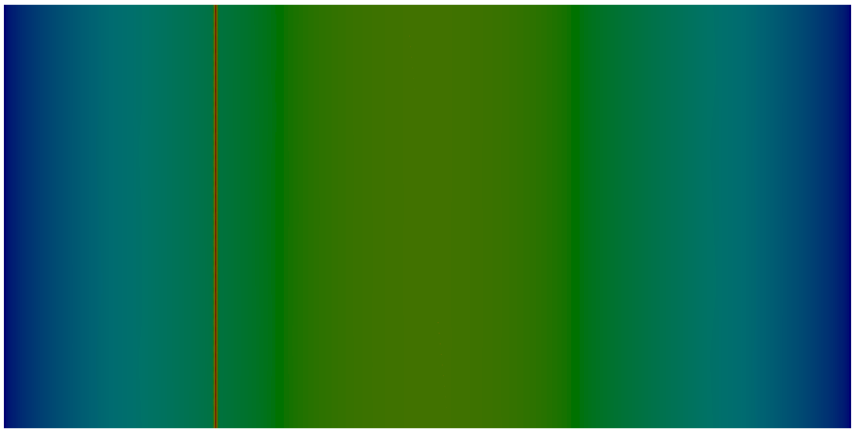

(a) Solution of initial global problem in *IGw/S-II* strategy. This is the solution of the enriched global problem in the *IGw/S* strategy (Cf. Section 6.1).

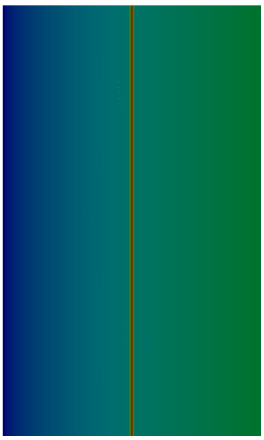

(b) Solution of local problem.

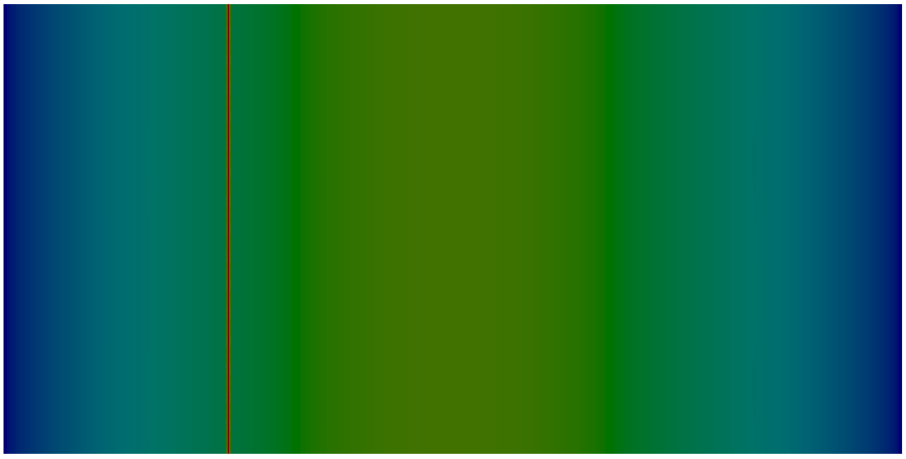

(c) Solution of enriched global problem.

Figure 21: Temperature distributions computed in the initial global, local, and enriched global problems corresponding to global Mesh 2x and 13 levels of refinement in the local problem. The *IGw/S-II* strategy is used. The thermal spike is well resolved in the initial global problem and thus the local problem can also capture well this behavior.

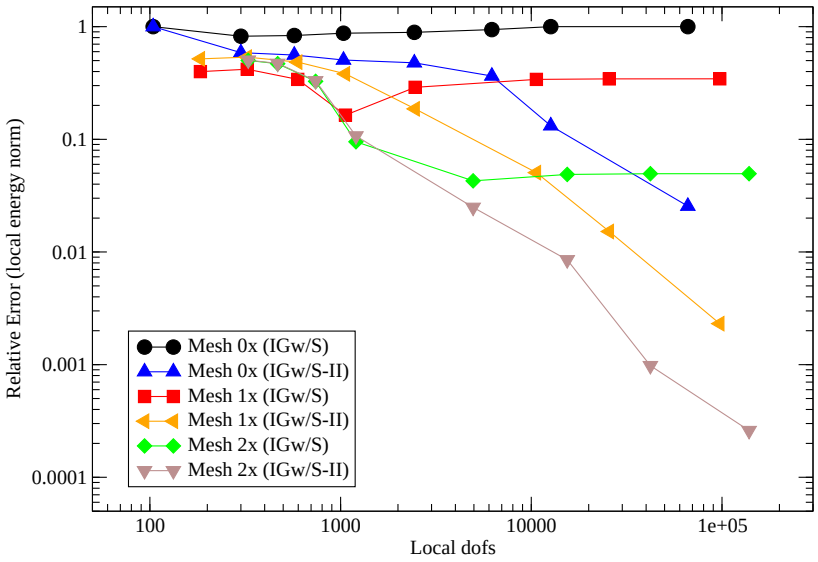

Figure 22: Relative error in energy norm for local problems in strategies *IGw/S* and *IGw/S-II*. The only difference in the local problems is the boundary conditions used.

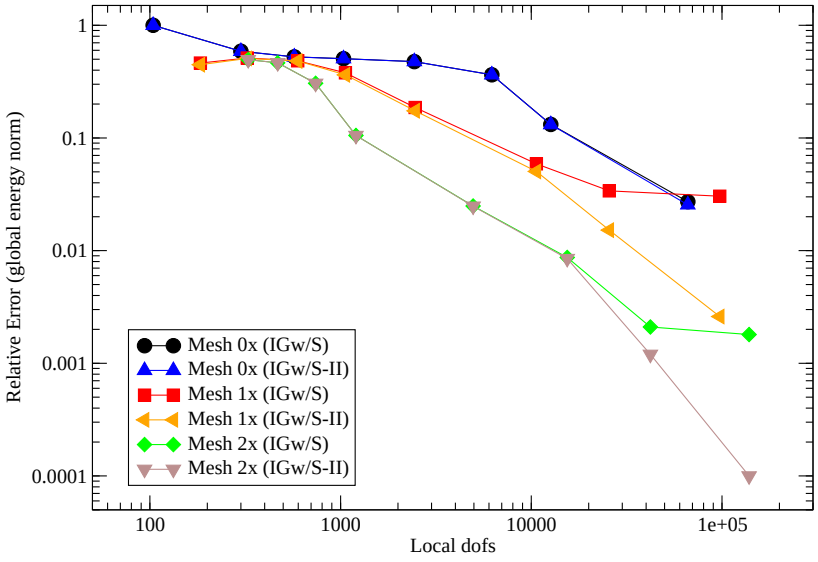

Figure 23: Relative error in energy norm for enriched global problems in strategies *IGw/S* and *IGw/S-II*.

6.3 Spike Absent from Initial Global Problem

In this section, we investigate another approach to improve the boundary conditions for the local problems and thus extend the range of target error level for the enriched global problem. In the strategy investigated here, the rough portion of the thermal loading applied to the initial global problem is removed. This idea is based on the fact that the spike in the temperature profile is very localized, and it has virtually no effect on the *exact* solution outside of a small neighborhood of the thermal spike. Therefore, as long as the local problem boundaries are not within a few millimeters of the temperature peak, the correct boundary conditions are essentially those from the smooth portion of the loading and the exponential portion will have no appreciable effect. For simplicity, this approach will be referred to as *Initial Global problem without Spike*, or *IGw/oS*.

Figure 24 shows the temperature distributions computed in the initial global, local, and enriched global problems of the *IGw/oS* strategy. The thermal spike is well resolved in both the local and enriched global problems even though it is absent in the initial global problem.

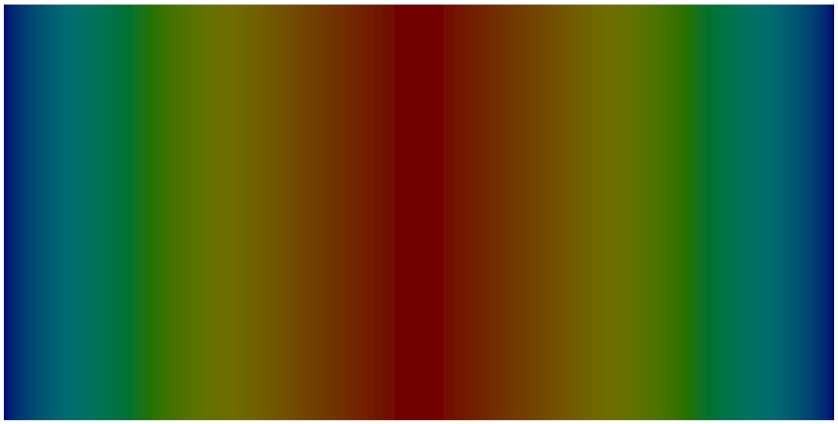

(a) Solution of initial global problem in *IGw/oS* strategy. The thermal spike is absent from this solution.

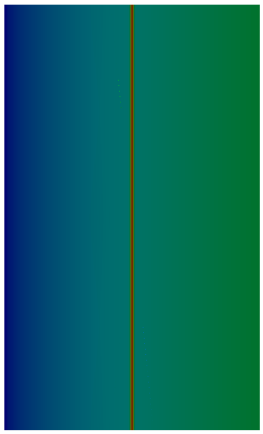

(b) Solution of local problem.

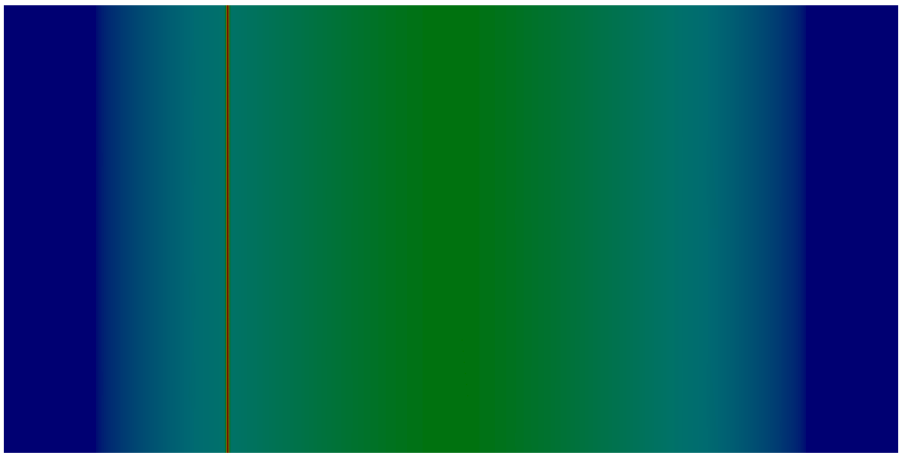

(c) Solution of enriched global problem.

Figure 24: Temperature distributions for initial global, local, and enriched global problems for *IGw/oS* strategy corresponding to global Mesh 2x, 13 levels of refinement in the local problem. Meshes 0x and 1x provide qualitatively similar results. The thermal spike is well resolved in both the local and enriched global problems.

Figures 25 shows the relative error in energy norm in the local problems in strategies *IGw/S* and *IGw/oS*. As in the case of strategy *IGw/S-II*, we can observe a dramatic improvement on the convergence behavior of the local solutions when strategy *IGw/oS* is used. In fact, the performance of strategies *IGw/oS* and *IGw/S-II* is very similar (Cf. Figure 22).

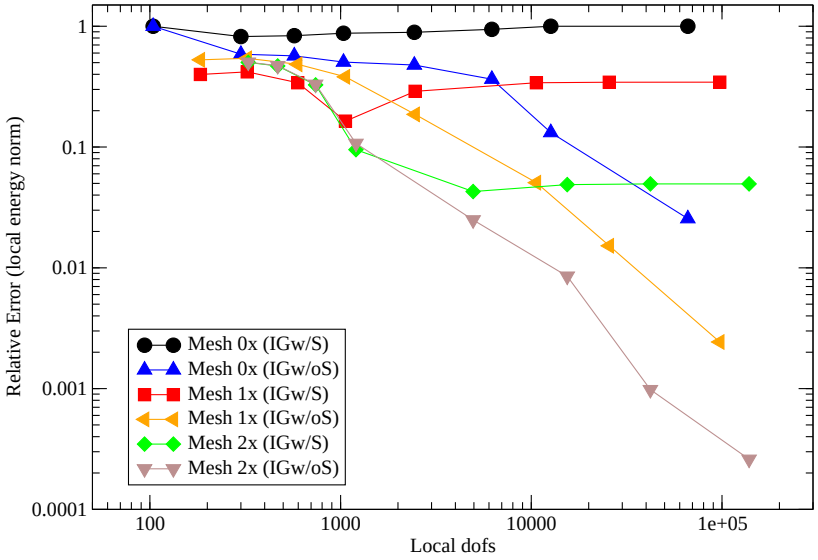

Figure 25: Relative error in energy norm for local problems in strategies *IGw/S* and *IGw/oS*. The only difference in the local problems is the boundary conditions used. In the case of *IGw/oS* strategy, The thermal spike was removed from the initial global domain.

Figure 26 shows the relative error in energy norm for enriched global problems in strategies *IGw/S* and *IGw/oS*. We can observe convergence of the enriched global solution computed with strategy *IGw/oS* over a larger range of target error level than in the case of *IGw/S* strategy.

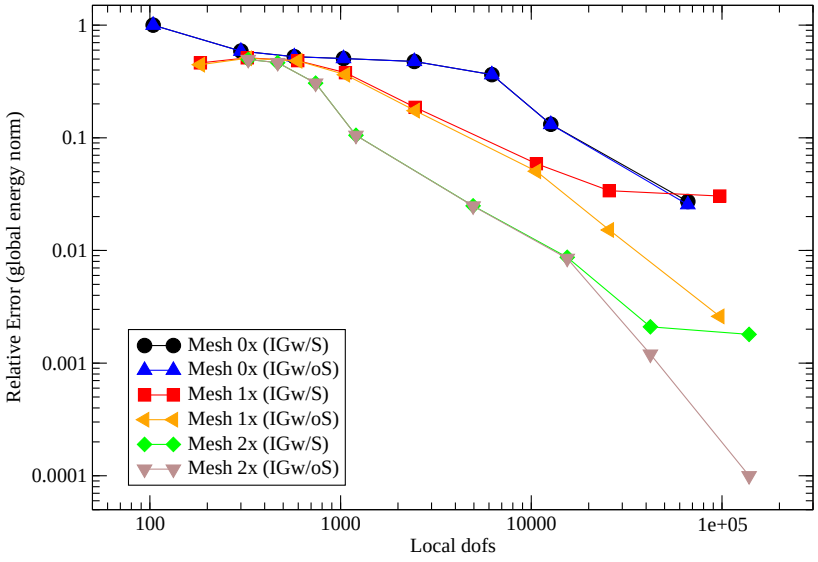

Figure 26: Relative error in energy norm for enriched global problems in strategies *IGw/S* and *IGw/oS*.

6.4 Effect of Enriching the Global Problem

The *GFEM*$^{g\text{-}l}$, as noted previously, differs from the traditional global-local FEM in that there is the added step of enriching the global domain with the local solution and re-solving the global problem. In this section, we compare the performance of these two methods for each of the strategies proposed in previous sections, i.e., *IGw/S*, *IGw/S-II* and *IGw/oS*.

Figure 27 compares the convergence in energy norm in the local and enriched global domains for strategy *IGw/S*. In these plots, there is a significant difference in the convergence rates as well as the error values between local and enriched global solutions. In some cases, the enrichment of the global domain can take local solutions which show no convergence behavior, and a large relative error, and convert this local information into a global solution which shows good convergence behavior, as well as significantly lower error values.

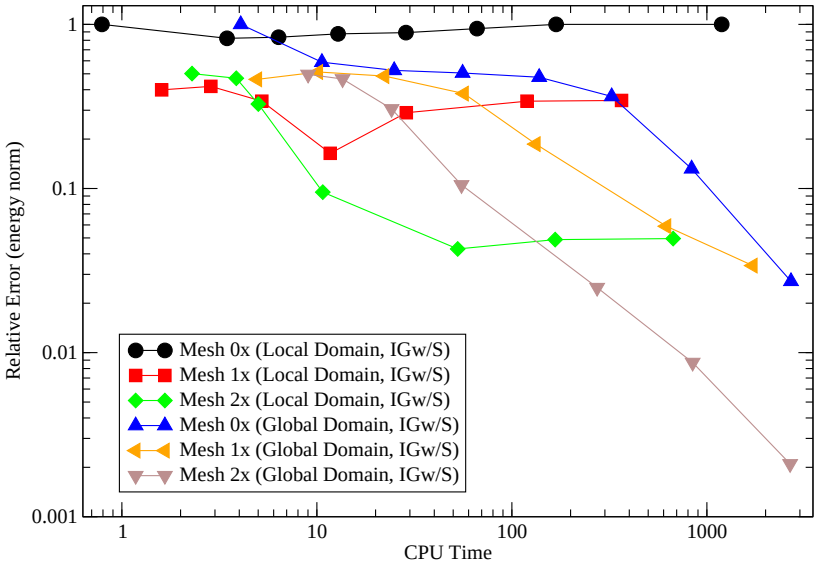

Figure 27: Comparison of convergence in energy norm in local and enriched global domains for *IGw/S* strategy.

Figures 28 and 29 compare the convergence in energy norm in the local and enriched global domains for strategy *IGw/S-II*. The local domains, in this case, are provided with good boundary conditions, and thus the local domains themselves do provide accurate solutions. As a result, the improvement is not as drastic as that seen in the *IGw/S* case. The only noticeable improvement is in the case of Mesh 2x and at low error levels (Cf. Figure 29). As was mentioned earlier, the scenario where a well-resolved spike is used in the initial global problem is of particular interest because it will be relied upon particularly in the transient setting, where the enriched global problem of one time step may be used to provide accurate boundary conditions for the local problem in the next time step. This methodology, if successful, will provide us with the ability to resolve very fine local features using a fixed, coarse global mesh throughout the entire transient analysis.

Figure 30 compares the convergence in energy norm in the local and enriched global domains for *IGw/oS* strategy. As in the *IGw/S-II* case, the local domains are provided with good boundary conditions, so the local domains are able to generate accurate solutions. As a result, the improvement is once again not as drastic as that seen in the *IGw/S* case.

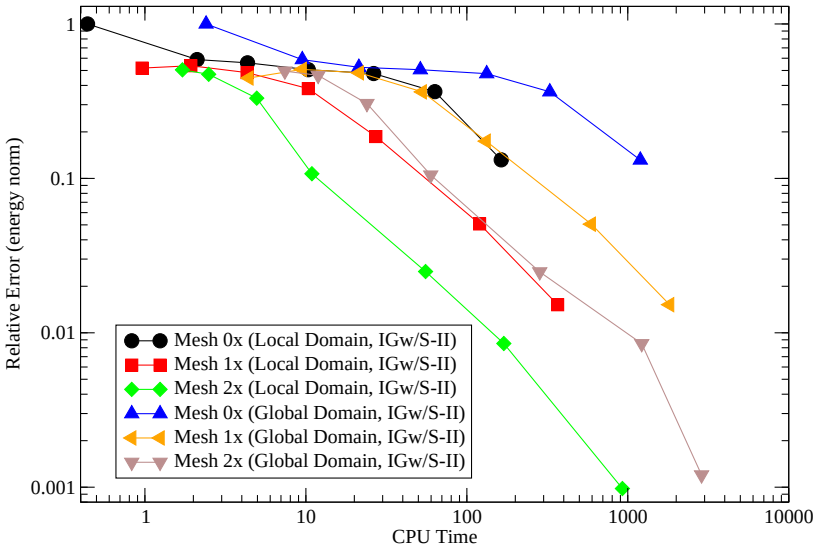

Figure 28: Comparison of convergence in energy norm in local and enriched global domains for *IGw/S-II* strategy.

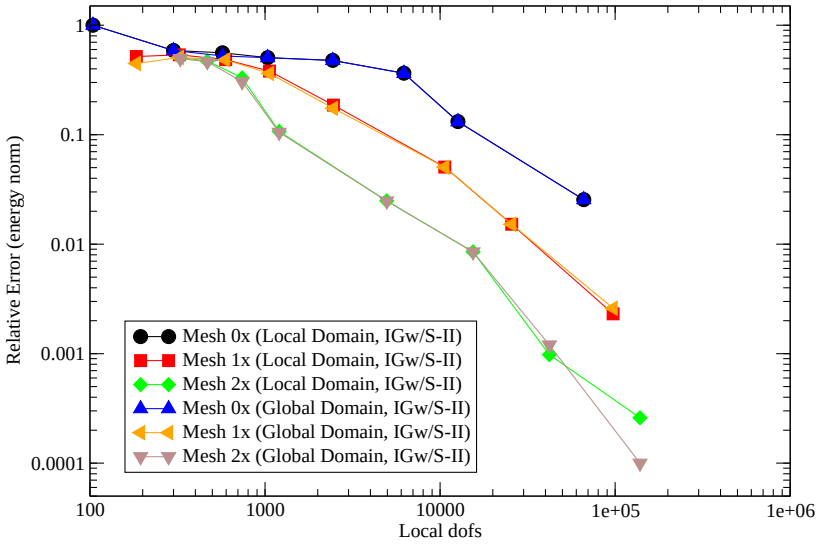

Figure 29: Data of Figure 28 plotted against the number of DOFs in the local problems. The plot includes data points that could not be included in Figure 28 due to a limitation of the function we use to measure CPU time.

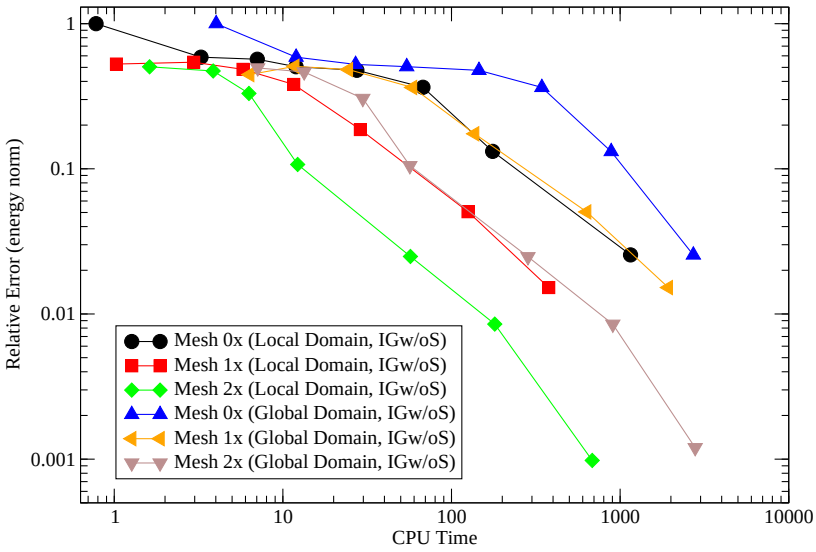

Figure 30: Comparison of convergence in energy norm in local and enriched global domains for *IGw/oS* strategy.

7 Conclusions

In this paper, the generalized FEM with global-local enrichments (*GFEM*$^{g\text{-}l}$) [14, 17, 28] is formulated for steady-state heat transfer problems with solutions exhibiting highly localized sharp thermal gradients. The proposed method is related to the classical global-local FEM (*GL-FEM*) [11, 21, 33] which is broadly used in the industry. They share several attractive features like

(i) the possibility of capturing localized solution features using uniform, coarse, global meshes. This removes, for example, the need to refine global meshes that are usually complex and very large. A single global mesh can be used to analyze the effect of localized thermal loads at different parts of a structure. All that is needed is the computation of local solutions and the hierarchical enrichment of the global solution space. Additional computational implications of this feature of the *GFEM*$^{g\text{-}l}$ are discussed in Section 4.1 and in [14];

(ii) the size of the enriched global problem is about the same as the initial global problem and it does not depend on the size or discretization used in the local problems;

(iii) while not explored in this paper, it is conceivable to use in the *GFEM*$^{g\text{-}l}$ different approximation methods to solve the global and local problems, like in the *GL-FEM*. *Hp* adaptive finite elements methods [8, 9, 10, 34, 38, 39], for example, would be an excellent option for solving the local problems;

(iv) the solution of multiple local problems can be parallelized without difficulty allowing the solution of large problems very efficiently. The parallelization of the *GFEM*$^{g\text{-}l}$ is the subject of a forthcoming paper;

(v) the *GL-FEM* uses the same variational principle as the original problem and thus no stability issues are introduced by the method.

While the *GFEM*$^{g\text{-}l}$ share many of the attractive features of the *GL-FEM*, the numerical experiments presented here and in [14, 28], demonstrate that the *GFEM*$^{g\text{-}l}$ is much more robust than the *GL-FEM*. The

former was able to deliver accurate global solutions even when limited or no convergence was observed in the local problems. The errors in the enriched global problem were, in some cases, orders of magnitude smaller than in the local problems. The difficulties of the *GL-FEM* with the class of problems investigated here is due to the large errors of global solutions computed on coarse meshes. This is illustrated in Figure 12 which shows that the discretization error may be large even far from the thermal spike.

The numerical experiments presented here also demonstrate that the information transfer between local (fine) and global (coarse) scales using the partition of unity framework is very effective (Cf. Section 6.4). We show that the global problem converges at least as fast as the local problems and in many cases the enriched global problem can deliver much more accurate solutions than the local ones.

Acknowledgments: The authors gratefully acknowledge the contributions of the Midwest Structural Sciences Center (MSSC) at the University of Illinois at Urbana-Champaign. The Center is supported by the U.S. Air Force Research Laboratory Air Vehicles Directorate under contract number FA8650-06-2-3620.

References

[1] I. Babuška and J.M. Melenk. The partition of unity finite element method. *International Journal for Numerical Methods in Engineering*, 40:727–758, 1997.

[2] I. Babuška, G. Caloz, and J.E. Osborn. Special finite element methods for a class of second order elliptic problems with rough coefficients. *SIAM Journal on Numerical Analysis*, 31(4):745–981, 1994.

[3] I. Babuška, F. Ihlenburg, E. Paik, and S. Sauter. A generalized finite element method for solving the Helmholtz equation in two dimensions with minimal pollution. *Computer Methods in Applied Mechanics and Engineering*, 128(3–4):325–360, 1995.

[4] I. Babuška, U. Banerjee, and J.E. Osborn. Survey of meshless and generalized finite element methods: A unified approach. *Acta Numerica*, 12:1–125, May 2003.

[5] H. K. Ching and J. K. Chen. Thermomechanical analysis of functionally graded composites under laser heating by the MLPG method. *Computer Modeling in Engineering and Sciences*, 13(3):199–217, 2006.

[6] A. Combescure, A. Gravouil, D. Gregoire, and J. Rethore. X-FEM a good candidate for energy conservation in simulation of brittle dynamic crack propagation. *Computer Methods in Applied Mechanics and Engineering*, 197:309–318, 2008.

[7] D. D'Ambrosio. Numerical prediction of laminar shock/shock interactions in hypersonic flow. *Journal of Spacecraft and Rockets*, 40(2):153–161, 2003.

[8] L. Demkowicz. *Computing with Hp-Adaptive Finite Elements, Vol. 1: One and Two Dimensional Elliptic and Maxwell Problems*. Chapman & Hall/CRC, 2006.

[9] L. Demkowicz, J. T. Oden, W. Rachowicz, and O. Hardy. Toward a universal *h-p* adaptive finite element strategy, Part 1. Constrained approximation and data structure. *Computer Methods in Applied Mechanics and Engineering*, 77:79–112, 1989.

[10] L. Demkowicz, J. Kurtz, D. Pardo, M. Paszynski, W. Rachowicz, and A. Zdunek. *Computing with Hp-Adaptive Finite Elements, Vol. 2: Frontiers: Three Dimensional Elliptic and Maxwell Problems with Applications*. Chapman & Hall/CRC, 2007.

[11] A.Th. Diamantoudis and G.N. Labeas. Stress intensity factors of semi-elliptical surface cracks in pressure vessels by global-local finite element methodology. *Engineering Fracture Mechanics*, 72: 1299–1312, 2005.

[12] C.A. Duarte. *The hp Cloud Method*. PhD dissertation, The University of Texas at Austin, December 1996. Austin, TX, USA.

[13] C.A. Duarte and I. Babuška. Mesh-independent directional *p*-enrichment using the generalized finite element method. *International Journal for Numerical Methods in Engineering*, 55(12):1477–1492, 2002. http://dx.doi.org/10.1002/nme.557.

[14] C.A. Duarte and D.-J. Kim. Analysis and applications of a generalized finite element method with global-local enrichment functions. *Computer Methods in Applied Mechanics and Engineering*, 197 (6-8):487–504, 2008. http://dx.doi.org/10.1016/j.cma.2007.08.017.

[15] C.A. Duarte, I. Babuška, and J.T. Oden. Generalized finite element methods for three dimensional structural mechanics problems. *Computers and Structures*, 77:215–232, 2000.

[16] C.A. Duarte, O.N. Hamzeh, T.J. Liszka, and W.W. Tworzydlo. A generalized finite element method for the simulation of three-dimensional dynamic crack propagation. *Computer Methods in Applied Mechanics and Engineering*, 190(15-17):2227–2262, 2001. http://dx.doi.org/10.1016/S0045-7825(00)00233-4.

[17] C.A. Duarte, D.-J. Kim, and I. Babuška. Chapter: A global-local approach for the construction of enrichment functions for the generalized fem and its application to three-dimensional cracks. In V.M.A. Leitão, C.J.S. Alves, and C.A. Duarte, editors, *Advances in Meshfree Techniques*, volume 5 of *Computational Methods in Applied Sciences*, The Netherlands, 2007. Springer. ISBN 978-1-4020-6094-6.

[18] C.A.M. Duarte and J.T. Oden. Hp clouds–A meshless method to solve boundary-value problems. Technical Report 95-05, TICAM, The University of Texas at Austin, May 1995.

[19] C.A.M. Duarte and J.T. Oden. *Hp* clouds—An *hp* meshless method. *Numerical Methods for Partial Differential Equations*, 12:673–705, 1996.

[20] C.A.M. Duarte and J.T. Oden. An *hp* adaptive method using clouds. *Computer Methods in Applied Mechanics and Engineering*, 139:237–262, 1996.

[21] C.A. Felippa. Introduction to finite element methods., 2004. Course Notes. Department of Aerospace Engineeing Sciences, University of Colorado at Boulder. Available at http://www.colorado.edu/engineering/Aerospace/CAS/courses.d/IFEM.d.

[22] M. J. Frame and M. J. Lewis. Analytical solution of the type IV shock interaction. *Journal of Propulsion and Power*, 13(5):601–609, 1997.

[23] P. P. Friedmann, K. G. Powell, J. J Mcnamara, B. J. Thuruthimattam, and R. Bartels. Hypersonic aerothermoelastic studies for reusable launch vehicles, 2004. AIAA 2004-1590.

[24] P. P. Friedmann, K. G. Powell, J. J Mcnamara, B. J. Thuruthimattam, and R. Bartels. Three-dimensional aeroelastic and aerothermoelastic behavior in hypersonic flow, 2005. AIAA 2005-2175.

[25] C. E. Glass. Non-continuum hypersonic shock interactions on a simulated airbreathing engine cowl, 2003. AIAA 2003-3772.

[26] F. Ihlenburg. *Finite Element Analysis of Acoustic Scattering*. Springer-Verlag, New York, 1998.

[27] K. K. Kamma and K. C. Saw. Hierarchical *p*-version finite elements and adaptive *a posteriori* computational formulations for two-dimensional thermal analysis. *Computers and Structures*, 32(5):1183–1194, 1989.

[28] D.-J. Kim, C.A. Duarte, and J.P. Pereira. Analysis of interacting cracks using the generalized finite element method with global-local enrichment functions. *ASME Journal of Applied Mechanics*, 75(5), 2008. http://dx.doi.org/10.1115/1.2936240.

[29] W. Li, X. Deng, and A. J. Rosakis. Determination of temperature field around a rapidly moving crack-tip in an elastic-plastic solid. *International Journal of Heat and Mass Transfer*, 39(4):677–690, 1996.

[30] J.M. Melenk and I. Babuška. The partition of unity finite element method: Basic theory and applications. *Computer Methods in Applied Mechanics and Engineering*, 139:289–314, 1996.

[31] R. Merle and J. Dolbow. Solving thermal and phase change problem with the eXtended finite element method. *Computational Mechanics*, 28:339–350, 2002.

[32] J. R. Moselle, A. R. Wieting, M.S. Holden, and C. Glass. Studies of aerothermal loads generated in regions of shock/shock interaction in hypersonic flow, 1988. AIAA-88-0477.

[33] A.K. Noor. Global-local methodologies and their applications to nonlinear analysis. *Finite Elements in Analysis and Design*, 2:333–346, 1986.

[34] J. T. Oden, L. Demkowicz, W. Rachowicz, and T. A. Westermann. Toward a universal *h-p* adaptive finite element strategy, Part 2. A posteriori error estimation. *Computer Methods in Applied Mechanics and Engineering*, 77:113–180, 1989.

[35] J.T. Oden, C.A. Duarte, and O.C. Zienkiewicz. A new cloud-based *hp* finite element method. *Computer Methods in Applied Mechanics and Engineering*, 153:117–126, 1998.

[36] Patrick James O'Hara. Finite element analysis of three-dimensional heat transfer for problems involving sharp thermal gradients. Master's thesis, University of Illinois at Urbana-Champaign, 2007.

[37] M. E. Plesha, R. D. Cook, D. S. Malkus, and R. J. Witt. *Concepts and Applications of Finite Element Analysis*. John Wiley & Sons, New York, 2002.

[38] W. Rachowicz, J. T. Oden, and L. Demkowicz. Toward a universal *h-p* adaptive finite element strategy, Part 3. Design of *h-p* meshes. *Computer Methods in Applied Mechanics and Engineering*, 77:181–212, 1989.

[39] Ch. Schwab. *P- and hp- Finite Element Methods: Theory and Applications to Solid and Fluid Mechanics*. Oxford University Press, 1999.

[40] A. Simone, C.A. Duarte, and E. van der Giessen. A generalized finite element method for polycrystals with discontinuous grain boundaries. *International Journal for Numerical Methods in Engineering*, 67 (8):1122–1145, 2006. http://dx.doi.org/10.1002/nme.1658.

[41] M. L. Spearman. Lessons learned in the high-speed aerodynamic research programs of the *NACA/NASA*, 2005. AIAA 2005-0327.

[42] T. Strouboulis, K. Copps, and I. Babuška. The generalized finite element method. *Computer Methods in Applied Mechanics and Engineering*, 190:4081–4193, 2001.

[43] B. Szabo and I. Babuška. *Finite Element Analysis*. John Wiley and Sons, New York, 1991.

[44] E. A. Thornton, A. R. Wieting, and K. Morgan. Application of integrated fluid-thermal-structural analysis methods. *Journal of Thin-Walled Structures*, 11:1–23, 1991.

[45] T. L. Turner and R. L. Ash. Analysis of the thermal environment and thermal response associated with thermal-acoustic testing, 1990. AIAA-90-0975-CP.

[46] D. Y. Tzou. Fracture path emanating from a rapidly moving heat soucre - The effect of thermal shock waves under high rate response. *Engineering Fracture Mechanics*, 41(1):111–125, 1992.

[47] A. R. Wieting. Experimental study of shock wave interference heating on a cylindrical leading edge, 1987. NASA Technical Memorandum 100484.

[48] O. C. Zienkiewicz, R. L. Taylor, and J. Z. Zhu. *The Finite Element Method: Its Basis and Fundamentals*. Elsevier Butterworth-Heinemann, 2005.